Magnetic signatures of lunar impact craters

Xi Yang, Mark Wieczorek

Icarus 415 (2024) 116049

Contents lists available at ScienceDirect

Icarus

journal homepage: www.elsevier.com/locate/icarus

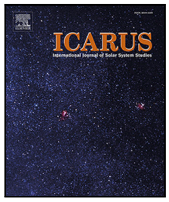

Research Paper

Magnetic signatures of lunar impact craters

Xi Yang [a,b,*], Mark Wieczorek [c]

[a] Institute of Geophysics, ETH Zürich, Sonneggstrasse 5, Zürich, 8092, Switzerland
[b] School of Earth and Space Sciences, Peking University, No. 5 Yiheyuan Road, Haidian District, Beijing, 100871, PR China
[c] Université Paris Cité, Institut de Physique du Globe de Paris, CNRS, 1 rue Jussieu, Paris, 75005, France

ARTICLE INFO

Keywords:
Lunar craters
Lunar magnetic fields
Magnetic anomalies

ABSTRACT

The Moon almost certainly had an internally generated magnetic field in its past, but the duration of the dynamo, its temporal stability, and the surface field intensity are poorly known. Impact cratering events heat portions of the crust above the Curie temperature, allowing the ambient magnetic field strength to be recorded as the crater cools. We systematically analyzed the magnetic signatures of lunar impact craters with diameters greater than 90 km using recent magnetic field models and crater databases. Craters were classified as having evidence for impact-related central magnetization or demagnetization, and synthetic magnetic field models were used to estimate the number of incorrect identifications. In total, about 15% of craters were found to have impact-related magnetized or demagnetized signatures. The proportion of pre-Nectarian and Nectarian aged craters in the magnetized class is about 2%–3%, and there is little evidence for magnetized craters in the Imbrian and younger periods. The percentage of craters in the demagnetized class is about 0.3%–3% in the pre-Nectarian and Nectarian periods and abruptly increases to 16% in the Imbrian period. Our observations are consistent with the presence of strong dynamo fields during portions of the older pre-Nectarian and Nectarian periods, with a weakening (or cessation) of the dynamo at the beginning of the younger Imbrian period. These results differ from paleomagnetic analyses of lunar samples that imply the existence of strong dynamo field strengths from the pre-Nectarian up until at least the first half of the Imbrian period.

1. Introduction

The hypothesis that the core of the Moon once generated a dynamo field is now widely accepted (for reviews, see Weiss and Tikoo, 2014; Wieczorek et al., 2022; Tikoo and Evans, 2022). Paleomagnetic analyses of lunar rocks show evidence for long-lived surface fields with Earth-like intensities between about 4.2 and 3.56 Ga (Garrick-Bethell et al., 2009, 2017; Weiss and Tikoo, 2014). Younger lunar samples show that these fields then weakened by an order of magnitude at some point before ~3.2 Ga (Tikoo et al., 2014) and that all dynamo activity ceased at some point between ~1.92 Ga and ~0.8 Ga (Mighani et al., 2020). Several mechanisms have been proposed for powering a lunar dynamo, including thermal convection (Evans et al., 2014; Laneuville et al., 2013), enhanced cooling during the foundering of Ti-rich magma-ocean cumulates (Evans and Tikoo, 2022), core crystallization (Zhang et al., 2013; Scheinberg et al., 2015; Laneuville et al., 2014, 2018), mechanical forcing (Dwyer et al., 2011; Cébron et al., 2019; Stys and Dumberry, 2020), non-synchronous rotation driven by impacts (Le Bars et al., 2011), and thermal convection in a basal silicate magma ocean (Scheinberg et al., 2018). However, there remain problems in reconciling the lunar dynamo models with the paleomagnetic measurements. Dynamo models cannot easily account for the high field strengths predicted by the paleomagnetic analyses (e.g., Evans et al., 2018; Wieczorek et al., 2022), and it is not clear if the dynamo operated in a continuous or episodic manner. Furthermore, one recent paleomagnetic study has even suggested that there was no long-lived dynamo field at all after about 4 Ga (Tarduno et al., 2021).

When the crust of the Moon cools in the presence of an ambient magnetic field, it can acquire a remanent magnetization and generate a magnetic anomaly that can be detected from orbit. Measurements made by the Apollo 15 and 16 subsatellite magnetometers, as well as during the later Lunar Prospector and Kaguya missions, show that the lunar crust is heterogeneously magnetized over scales of tens to a few hundred kilometers in size (e.g., Dyal et al., 1974; Mitchell et al., 2008; Tsunakawa et al., 2015; Ravat et al., 2020a; Arkani-Hamed and Boutin, 2014). Strong magnetic anomalies are found at many places on the lunar surface, though most of these are not easily correlated with known geologic processes, such as the enigmatic Reiner Gamma anomaly (e.g., Hemingway and Tikoo, 2018). The depth to the top

* Corresponding author at: Institute of Geophysics, ETH Zürich, Sonneggstrasse 5, Zürich, 8092, Switzerland.
E-mail addresses: xiyang1@student.ethz.ch (X. Yang), mark.wieczorek@cnrs.fr (M. Wieczorek).
URL: https://markwieczorek.github.io/website/ (M. Wieczorek).

https://doi.org/10.1016/j.icarus.2024.116049
Received 9 January 2024; Received in revised form 8 March 2024; Accepted 12 March 2024
Available online 15 March 2024

of the magnetic sources in the lunar crust is estimated to vary from the surface to about 25 km, with most of the weak sources being deeper than 10 km below the surface (Wieczorek, 2018b). On a global scale, two prominent regions with low magnetic field strength are also observed. The largest of these is on the nearside and encompasses the Imbrium basin, a part of Oceanus Procellarum, and the surrounding highlands. This region is similar in extent to the Procellarum KREEP (an acronym for potassium, rare-earth elements, and phosphorous rich rocks) Terrane, which suggests that large portions of the crust there had temperatures above the magnetic Curie temperature when the strong dynamo fields were present (Wieczorek, 2018b; Laneuville et al., 2018). The other magnetic low is located on the northern farside highlands and has no obvious explanation.

Impact cratering is one geological process that could either magnetize or demagnetize the crust throughout lunar history. During an impact event, portions of the crust would be heated above the Curie temperature of iron metal, which is the most prominent magnetic mineral in lunar rocks. These heated materials would lose their pre-existing magnetization, but they could acquire new magnetization if an ambient magnetic field was present when they cooled. The impact event would also excavate and remove any pre-existing magnetic materials from within the crater rim, and deposit these materials with randomized directions in the surrounding ejecta (e.g., Lillis et al., 2013b). The shock wave that propagates from the impact point is also capable of either magnetizing or demagnetizing lunar rocks (Bezaeva et al., 2007; Gattacceca et al., 2008; Bezaeva et al., 2010; Gattacceca et al., 2010), depending on whether an ambient field was present at the time or not. Impact events can deliver large quantities of iron metal to the otherwise metal-poor lunar crust (Wieczorek et al., 2012; Oliveira et al., 2017), and some magnetic anomalies have been shown to have a positive correlation with topography and free-air gravity, indicating that they could perhaps be associated with shallow iron-rich impact ejecta (Gong and Wieczorek, 2020).

Previous studies have investigated the magnetic signatures of large impact basins on the Moon, whose diameters are typically hundreds of kilometers in size (Halekas et al., 2003; Le Bars et al., 2011; Hood, 2011; Hood and Spudis, 2016; Oliveira et al., 2017). Among the largest multi-ring basins, only five Nectarian basins are unambiguously associated with central magnetic anomalies, and the associated magnetizations are plausibly the result of iron-rich projectile materials incorporated into the basin impact melt sheet (Oliveira et al., 2017; Hood et al., 2021a). Basin magnetization is either ambiguous or absent in the older pre-Nectarian and younger Imbrian basins, which is surprising given that paleomagnetic analyses show evidence of strong dynamo fields during both of these geological periods. A large concentration of strong magnetic anomalies is located on the farside of the Moon near the equator, and this has been argued to be either the result of the deposition of iron-rich impact ejecta from an oblique South Pole-Aitken impact event (Wieczorek et al., 2012) or the short-lived amplification of ambient fields near the antipodes of the Imbrium, Serentitatis, and Crisium basins (see Hood and Artemieva, 2008; Oran et al., 2020). Most impact basins with impact-related demagnetization signatures possess a magnetic low that extends from the center to almost 2 crater radii (Halekas et al., 2003), and for smaller lunar craters with diameters larger than 50 km, the magnetic lows can in some cases extend to 2–4 crater radii (Halekas et al., 2002). These observations have been used to suggest that shock demagnetization rather than thermal demagnetization is responsible for the magnetic lows associated with some impact craters and basins.

In this study, we systematically analyzed the magnetic signatures of lunar impact craters using the most recent crater databases and global magnetic field models. All craters that are resolvable in the magnetic field models were considered, from large complex craters to multi-ring basins, and the likelihood that the magnetic signature was related to the impact event or other processes was assessed. From this analysis, we then investigated the history of the lunar dynamo and the origin of the crater magnetic signatures. We start in Section 2 by designing a classification scheme of crater magnetic signatures. Next, in Section 3, we analyze our database of craters in terms of crater size, age, and location, and also assess the azimuthally-averaged radial magnetic profiles of these craters. In Section 4, we compare our results with previous studies, discuss how our results may help in constraining the time evolution of the lunar dynamo, and discuss the mechanisms that could account for the observed impact-related magnetization and demagnetization signatures of lunar impact craters. Finally, we summarize the conclusions of this work in Section 5.

2. Data and methods

The Lunar Prospector spacecraft (1998–1999) made magnetometer and electron reflectometer measurements from a polar orbit at about 100 km altitude during its primary mission (Binder, 1998; Lin et al., 1998). During the extended phase of the mission, the spacecraft periapse was lowered and measurements were then made at an average altitude of about 30 km with a range from 11–66 km. Subsequent magnetometer measurements were made by the Kaguya mission (2007–2009) which collected data initially at an altitude of about 100 km and then later from 9–80 km during its low-altitude phase (Tsunakawa et al., 2010). All modern global magnetic field models of the Moon are based on using subsets of data acquired from these two missions.

Tsunakawa et al. (2015) developed a surface field model by combining low altitude (10–45 km) vector magnetic field measurements from the Lunar Prospector and Kaguya missions, and by removing the external field with a detrending procedure. Their inversion results provided a global three-component magnetic field model on the surface with a spatial resolution of 0.2°, which corresponds to ~6 km on the equator. This global model allowed for the construction of a spherical harmonic model with a maximum spherical harmonic degree of 450, which can resolve wavelengths as small as 25 km. Following this study, Ravat et al. (2020a) developed a global magnetic field model at the lunar surface by using along-track magnetic field gradients and by making use of an L1-norm regularization approach. The spatial resolution of their model is 0.1°, but we find that the signal strength decreases with respect to the model of Tsunakawa et al. (2015) beyond about spherical harmonic degree 200, which corresponds to a wavelength of about 55 km. Most recently, Hood et al. (2021b) and Hood et al. (2022) developed a magnetic field model that relied on a careful selection of the raw magnetic field measurements. By using only the radial component of detrended magnetic field measurements combined with an equivalent source dipole inversion, a global field model was developed at an altitude of 30 km above the surface. Gridded data were provided with a spacing of about 0.5°, but the effective horizontal resolution of their model was estimated to be about 60 km.

In this study, we used the surface vector field model of Tsunakawa et al. (2015) as our primary dataset, and the surface vector field model of Ravat et al. (2020a) was then used to confirm the magnetic signatures of the investigated craters. We did not use the Lunar Prospector electron reflectometer measurements (Mitchell et al., 2008) because the sparse nature of this dataset makes it difficult to compare directly with the global field models when analyzing individual impact craters. The total magnetic field strength was used for all our analyses, which was computed from the spherical harmonic coefficients of the two models at the mean radius of the Moon. Magnetic anomalies often have different expressions at spacecraft altitudes than at the surface (e.g., Ravat, 2011), and this could adversely affect the classification of impact crater magnetic signatures when using magnetic field maps far above the surface (see Figure S1 as an example). Nevertheless, we also assessed the magnetic signatures of the craters in our study at 30 km altitude using the vector field models of Tsunakawa et al. (2015), Hood et al. (2021b) and Hood et al. (2022). In addition to the magnetic field model, topography and shaded relief maps based on the Lunar Orbiter Laser Altimeter (LOLA) Digital Elevation Model

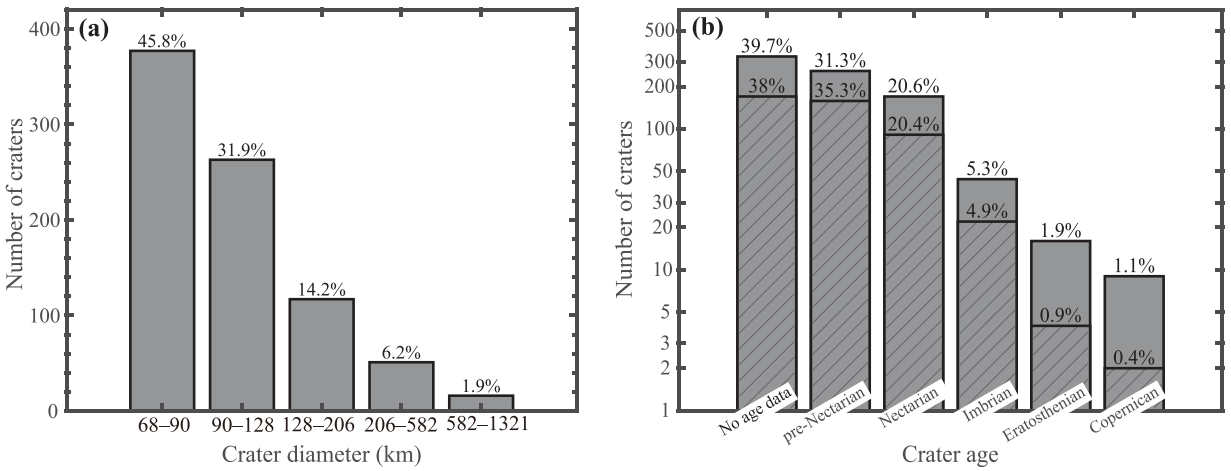

Fig. 1. The number of craters analyzed in this study is shown as a function of (a) crater diameter and (b) crater age. The number above each bar gives the percentage of craters in the interval. The diameter intervals are open for the lower bound and closed for the upper bound. The transparent cross-hatching in panel (b) is used to denote the number and percentages of craters with diameters greater than 90 km. The total number of craters that were analyzed with diameters greater than 68 and 90 km is 824 and 447, respectively.

(DEM) with a resolution of 128 pixels per degree were consulted to provide geological context. For example, some craters were found to be superposed by younger craters, buried by basaltic lavas, or were found to be asymmetric in crater morphology.

When classifying the magnetic signatures of impact craters, we made use of two different impact crater databases. For our primary database, we used the crater coordinates and diameters from Robbins (2019), which are based on images taken from the Lunar Reconnaissance Orbiter and Kaguya missions. This database was then supplemented with the peak-ring and multi-ring basins in the database of Neumann et al. (2015) that were characterized using gravity data from the Gravity Recovery and Interior Laboratory (GRAIL) mission and topography data from the Lunar Reconnaissance Orbiter mission. The peak ring basins in this latter database have diameters that range from 207 to 582 km, with the smallest multi-ring basin having a diameter of 571 km. For simplicity, we will treat the peak-ring to multi-ring basin transition occurring at a diameter of 582 km, which only misclassifies the smallest multi-ring basin, Hertzsprung, as a peak-ring basin. When the same impact basin was found in both datasets, we preferred the diameters and coordinates of Neumann et al. (2015). The South Pole-Aitken impact basin, which is the largest and oldest confirmed lunar impact basin, was not included in our study because of its geologic complexity and the fact that several basins formed subsequently in its interior. For each crater, we attempted to assign a geologic period for its formation age using the ages tabulated in an updated version of the crater database of Losiak et al. (2015) that is based on previous geological mapping studies.

The statistics of the crater diameters and ages used in our study are presented in Fig. 1. We initially considered all craters with diameters D greater than 68 km, except for the giant South Pole-Aitken basin. There are a total of 824 craters in our dataset, of which the largest is the Imbrium basin with a diameter of 1321 km. About 46% of the craters have diameters less than 90 km, about 46% have diameters between 90 and 206 km, and the remaining 8% (67 in number) have diameters greater than 206 km (Fig. 1a). In terms of age, 31% are from the oldest pre-Nectarian period, 21% are Nectarian, 5% are Imbrian, and 3% are from the youngest Eratosthenian and Copernican periods (Fig. 1b). The remaining 40% of craters in our database have no age data. Later in this manuscript, we will make use only of those craters whose diameters are greater than 90 km, of which there are 447. The age distribution for this diameter subset is plotted in Fig. 1b using cross-hatching.

In analyzing the impact-related magnetic signatures of lunar craters, we categorized them into three primary classes: magnetized (those craters with a central magnetic high that was caused by the impact), demagnetized (those with a central magnetic low that was caused by the impact), and no signal (those with no clear magnetic signal that was caused by the impact event). Given that the sizes of the craters in our analysis are at least several times the thickness of the magnetic layer in the crust, craters with central magnetic highs or lows imply the existence of a net excess or deficit of magnetization within the crater with respect to their surroundings. The signal fidelity of each crater in the magnetized and demagnetized classes was then further divided into three levels: certain, probable, and possible. This signal fidelity level represents a subjective assessment of how confident the analyst was in assigning the primary class and is an indicator of whether the observed magnetic signature is genetically related to the impact crater or not.

The characteristics of each classification are detailed in Table 1, and typical examples of craters in the magnetized and demagnetized classes are shown in Fig. 2. Certain craters (as shown in Fig. 2a,b) are those with a magnetic high or low in the crater interior that is symmetric, close to the crater center, and visually different from the surrounding terrain. Probable craters (as shown in Fig. 2c,d) have a magnetic signature that is somewhat more ambiguous. The magnetic high or low is either not symmetric with the crater topography or there is some doubt that the magnetic signature is different from the surroundings. Possible craters (as shown in Fig. 2e,f) have a magnetic signature that is only marginally different from the surroundings. For these craters, the magnetic signature is only more likely than not to be genetically related to the impact crater. No signal craters might have a magnetic high or low within the crater rim (as shown in Fig. 2g,f), but, such a signature is not considered to be caused by the impact event that formed the crater.

The decrease in fidelity level from certain to possible to no signal could be a result of several factors. First, there could be deficiencies in the surface magnetic field models that could give rise to fortuitous signals within the crater. Such signals could arise from data gaps, noise, or unmodeled external fields. Second, geologic processes that occurred after the crater formed could have given rise to magnetic anomalies that were located within the crater rim by chance. Such processes could include the emplacement of magmatic intrusions in the crust or the deposition of magnetized impact basin ejecta on top of the crater. Third, there could be pre-existing magnetic anomalies deep in the crust beneath the crater that were not reset by the impact event. Lastly, we note that as the strength of the magnetic anomaly in the crater interior decreases, it becomes more difficult for the analyst to classify the crater.

To assess the likelihood that the impact-related crater magnetic signatures were correctly classified, and to estimate the number of incorrect identifications that we might expect for each class, we made use of synthetic magnetic field models that were known to have no genetic relation to the impact craters in our analysis. In particular,

Table 1
Classification of impact crater magnetic signatures.

Signal fidelity	Crater type	
	Magnetized	Demagnetized
Certain	Impact craters with a magnetic high in the crater interior that is symmetric, close to the crater center, and visually different from the surroundings. The central magnetic high may also be surrounded by a magnetic low that extends to the crater rim and that truncates pre-existing magnetic signals. The origin of the magnetic signature is interpreted to be certainly related to the impact event that formed the crater.	Impact craters with a magnetic low in the crater interior that is symmetric and visually different from the surroundings. The magnetic low usually extends to the crater rim, may extend up to a few crater radii beyond the rim, and may truncate pre-existing magnetic signals. The origin of the magnetic signature is interpreted to be certainly related to the impact event that formed the crater.
Probable	Impact craters with a magnetic high in their interior where there is some doubt that the magnetic signature is different from the surrounding terrain. In comparison to certain craters, the central magnetic high might be smaller in amplitude, might not be located in the crater center, and might not be symmetric. The origin of the magnetic signature is interpreted to be only probably related to the impact event that formed the crater.	Impact craters with a magnetic low in their interior where there is some doubt that the magnetic signature is different from the surrounding terrain. The magnetic low might be found only in a portion of the crater, it might not be located in the crater center, or it might not be symmetric. The origin of the magnetic signature is interpreted to be only probably related to the impact event that formed the crater.
Possible	Impact craters where the magnetic signature is only marginally different from the surrounding terrain. In comparison to probable craters, the magnetic high might be smaller in amplitude, it might be close to the crater rim, and it might be separated into multiple weak anomalies. The origin of the magnetic signature is interpreted to be only possibly related to the impact event that formed the crater.	Impact craters with a magnetic low in its interior where there is considerable doubt that the magnetic signature is different from the surrounding terrain. In comparison to probable craters, the magnetic low might not show a clear boundary with the background, it might be highly asymmetric, and its area may extend considerably outside of the crater rim. The origin of the magnetic signature is interpreted to be only possibly related to the impact event that formed the crater.
No signal	The magnetic signature is not visually different from the surroundings or it is uncertain how to classify the crater. Any magnetic lows or highs within the crater rim are interpreted to be unrelated to the impact event that formed the crater.	

we addressed the following question: If the lunar magnetic field was unrelated to the craters in our analysis, how often would we expect to find a crater with an apparent magnetized or demagnetized signature by chance? Such a signature could arise, for example, by the fortuitous emplacement of magmatic intrusions within an impact crater that either became magnetized as they cooled in the presence of a global magnetic field, or that thermally demagnetized the crust in the absence of a global field. A magnetized signature could also occur by the fortuitous deposition of distant impact basin ejecta within a crater that became magnetized by cooling in the presence of a global magnetic field.

Since most magnetic anomalies on the Moon are unrelated to impact craters, we generated our synthetic magnetic field maps by rotating the geographic coordinate system of the observed fields. This ensures that the statistical properties of the real and synthetic maps are identical. The coordinate frame was rotated by using the standard Euler angles (α, β, γ), where the second rotation is defined with respect to the x axis. Given the amount of effort it takes to classify all of the craters in our study, we only considered two synthetic maps for each magnetic field model using the Euler angle sets (190°, 170°, 170°) and (180°, 180°, 180°). These sets of Euler angles maintain the predominant global feature of the lunar magnetic field where the strongest anomalies are located on the farside of the Moon. For each impact crater that we analyzed, we first classified the magnetic signature of the crater using the real magnetic field models, and then also classified the magnetic signature at the same location using the synthetic (rotated) magnetic field models. We note that different approaches have been used for classifying the magnetic signatures of impact craters on the Moon (e.g., Halekas et al., 2002, 2003; Hood, 2011), Mars (e.g., Lillis et al., 2008, 2010, 2013a; Vervelidou et al., 2017), and Earth (e.g., Pilkington and Grieve, 1992; Isac et al., 2016). However, these prior investigations either did not assess the possibility that the observed magnetic anomaly could be genetically unrelated to the impact structure or focused solely on impact demagnetization signatures.

Fig. 3 shows an example of the steps taken when analyzing each crater, in particular for the crater previously presented in Fig. 2b. In the first column, we plot the magnetic field strength of the Tsunakawa et al. (2015) model using a linear and logarithmic scale (upper and lower rows, respectively). To assess the uncertainties in the magnetic field models, the second column plots similar maps using the magnetic field model of Ravat et al. (2020a). The crater topography (Fig. 3c), along with a shaded relief map generated from the surface topography (Fig. 3h), are displayed in the middle column to help determine whether the magnetic anomalies are related to the impact crater, or if the magnetic anomaly was affected by later geological processes. Finally, to assess the likelihood of incorrectly classifying a crater, we made use of synthetic magnetic field models that were derived by rotating the coordinate systems of the Tsunakawa et al. (2015) and Ravat et al. (2020a) models with the first set of Euler angles (190°, 170°, 170°). The last two columns plot the magnetic field strength of these synthetic magnetic field models using linear and logarithmic scales, similar to those of the first two columns. A similar set of images as in Fig. 3 (not shown) was also generated using the second set of Euler angles (180°, 180°, 180°).

For each crater, images like that of Fig. 3 were produced, and the magnetic signature classifications using the real and synthetic magnetic field models were evaluated at the same time. As described in the following section, two analysts assessed the data independently and the classifications derived from the synthetic magnetic field models were used to quantify the expected number of false identifications for each class. The number of false identifications was then used to debias the number of craters in each class obtained using the real data and was also used to help determine the minimum crater diameter that could be classified reliably. The results using the 30 km altitude magnetic field maps were found to be broadly similar to those using the surface maps, and since the surface data are more appropriate for our analyses, the figures that make use of the 30 km altitude maps are presented in the supplemental materials.

3. Results

In this section, we first discuss how we constructed a debiased database of impact craters with impact-related magnetic signatures, and then report the statistical results of these craters as functions of crater diameter and age. In the second subsection, we analyze the spatial distribution of the craters in the magnetized and demagnetized classes. Finally, we assess the azimuthally averaged radial profiles of the magnetic field strength for craters in both the magnetized and demagnetized classes.

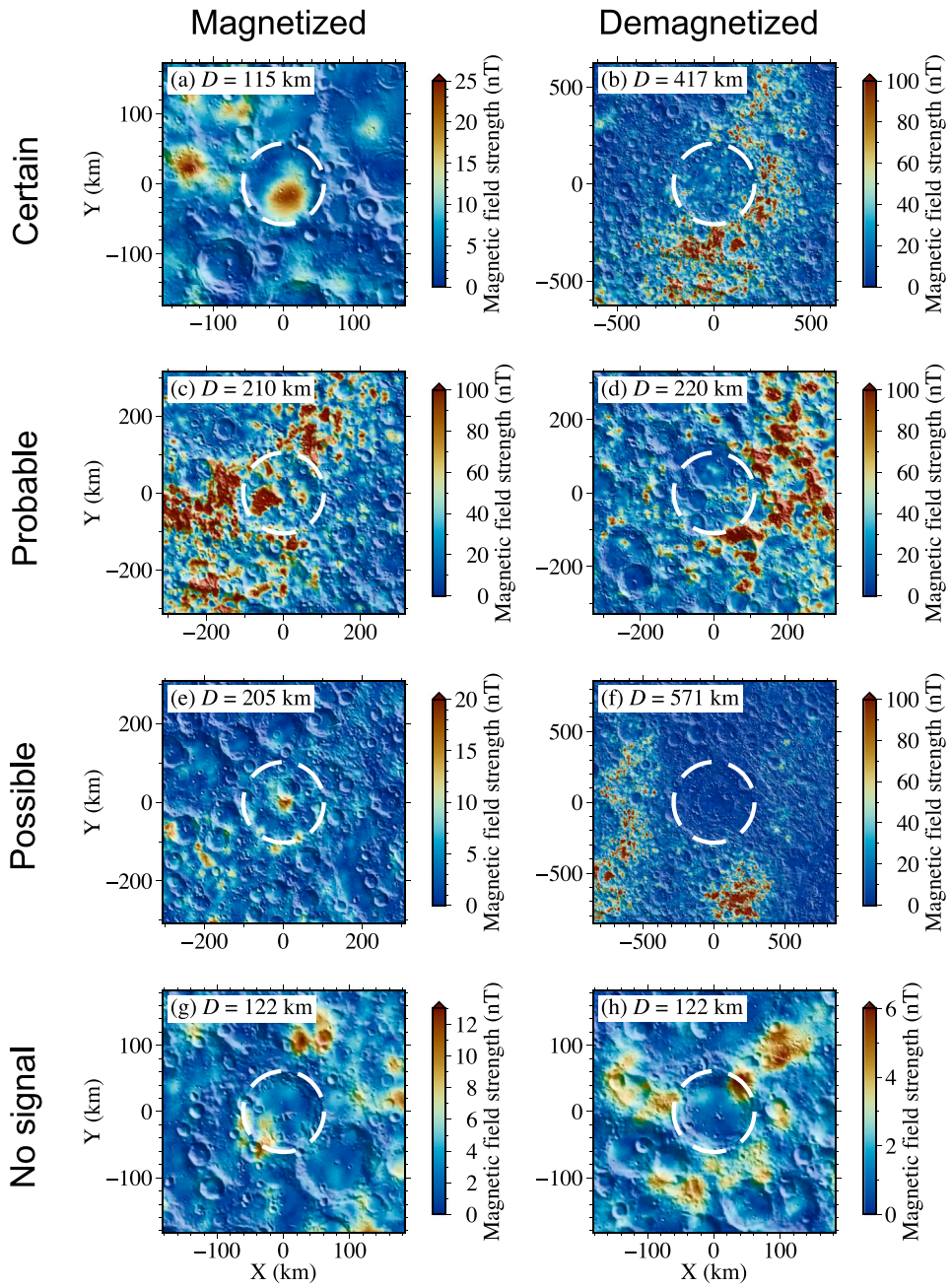

Fig. 2. Examples of craters with impact-related magnetic signatures based on the surface magnetic field strength from the model of Tsunakawa et al. (2015). Craters in the magnetized class are plotted in the left column and craters in the demagnetized class are plotted in the right column. From top to bottom, the rows correspond to certain, probable, and possible signal fidelities. The last row shows two examples of craters that were classified as having no signal, and whose magnetic signature is likely to be unrelated to the impact event that formed the crater. From (a) to (h), the displayed craters are Kastner, Korolev, Galois, TOPO-13, Bartels-Voskresenskiy, Hertzsprung, Nernst, and Carnot respectively, and the crater diameter D is provided for each crater. All maps are plotted using a Lambert azimuthal equal-area projection with the center of the projection corresponding to the crater center. The perceptually uniform Roma color map of Crameri et al. (2020) is used for this and all subsequent magnetic field strength figures.

3.1. Debiased database of craters with magnetic signatures

Given that the classification scheme we developed is somewhat subjective, the two authors of this manuscript categorized the crater magnetic signatures independently. Before performing the final classifications, the two analysts worked together to classify a small number of craters and tried to come to a consensus. Nevertheless, we found that each analyst had a slightly different threshold for including a crater in each of the classes listed in Table 1. Because of this, we attempted to remove the different biases of the two analysts by subtracting the number of false identifications they made using the synthetic magnetic field models. The rationale for this approach is that if one analyst was less restrictive and always classified more craters as having a certain magnetic signature, they would also classify more craters as having the same signature when using the synthetic data. Subtracting the two numbers would remove the bias.

For each analyst, we started by determining the number of craters for each class and signal fidelity level (e.g., possible magnetized craters), and these were then further subdivided by crater age and crater diameter ranges. The debiased number of craters was defined as the number of craters using the observed magnetic field models minus the number of craters using the synthetic magnetic field maps. For a few cases where the number of false identifications was greater than the number obtained using the real magnetic field models, we

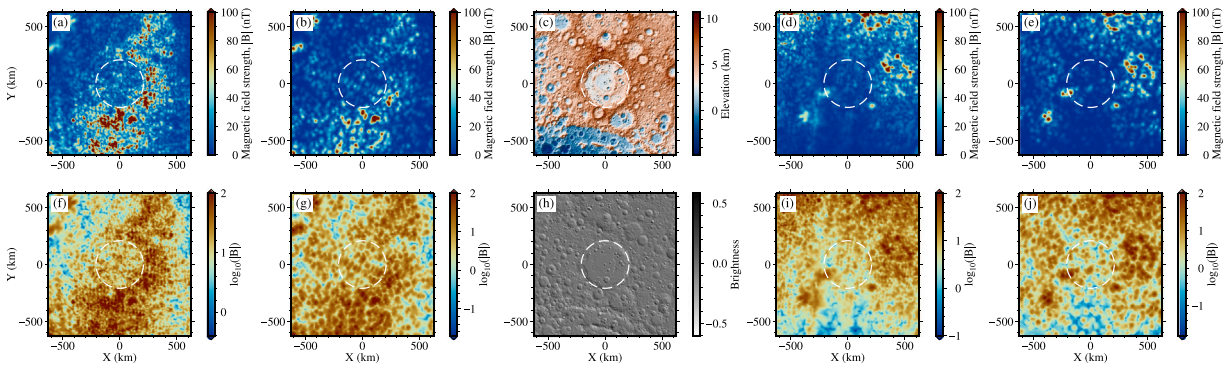

Fig. 3. An example of the datasets used to classify the impact-related magnetic signature of the 417 km diameter peak-ring basin Korolev. Shown are (a,f) the total magnetic field strength at the surface from the model of Tsunakawa et al. (2015) using linear and logarithmic scales, (b,g) similar maps as in the first column, but using the magnetic field model of Ravat et al. (2020a), and (c) crater topography and (h) shaded relief maps derived from the LOLA DEM. The last two columns (d,e,i,j) present magnetic field maps similar to the first two columns (a,b,f,g) but using synthetic (rotated) magnetic field models. Dashed circles represent the crater's main rim. All maps are plotted using a Lambert azimuthal equal-area projection with the center of the projection corresponding to the crater center.

set the debiased number of craters to zero. The debiased number of all craters in the magnetized or demagnetized classes of the analyst for the given diameter or age range was then defined as the sum of the debiased numbers of the three signal fidelities (debiased certain + debiased probable + debiased possible). The debiased percentage was then defined simply as the debiased number divided by the total number of craters in the given diameter or age range.

The classifications of the two analysts generally showed a good agreement. A total of 42 and 43 craters with diameters larger than 68 km were respectively classified as having an impact-related magnetized signature by the two analysts when using the real magnetic field models (Figure S2a). When using the two synthetic magnetic field maps, the average number of such craters was 30 and 31.5, respectively (Figure S2c and S3c). Considering craters in the 68–90 km diameter bin, both analysts found more craters in the magnetized class when using the synthetic magnetic field maps than when using the real maps. This suggests that magnetized crater signatures can only be classified reliably for crater diameters greater than 90 km. The difficulty of reliably detecting smaller craters with magnetized signatures is most likely a result of these craters having sizes that are comparable to the effective resolution of the magnetic field maps, which is somewhere between about 30 and 60 km.

In contrast to the magnetized class, the classifications of the two authors differed somewhat more for the demagnetized class. When considering craters larger than 90 km in size, the first analyst found 14 craters with impact-related demagnetization signatures, whereas the second found 22 (Figure S2b). This difference was somewhat mitigated when considering the average number of demagnetized craters that were found when using the two synthetic magnetic field models: The first analyst found an average of 1.5, whereas the second found 3.5 (Figure S2d and S3d).

In contrast to the magnetized craters, we note that both analysts found more demagnetized craters in the 68–90 km diameter bin when using the real magnetic field models than when using the synthetic models. Though this may indicate that craters with demagnetization signatures can be classified more reliably than craters with magnetized signatures for this diameter range, for the sake of consistency, we only considered craters with diameters greater than 90 km for both classes in our subsequent analyses.

Fig. 4 shows the percentages of craters in the magnetized and demagnetized classes after averaging the results of the two analysts when using both the real and synthetic magnetic field models. We plot our results using the percentage of each class, as opposed to the absolute number in each class, because there are naturally more small craters than large craters and more old craters than young craters. In the left panel, we group our results into four diameter bins, where the first two correspond to complex craters, and the following two correspond respectively to peak-ring and multi-ring basins. The division of the complex craters into two diameter bins of 90–128 and 128–206 km is arbitrary and was done solely to have a similar number of craters in each bin in this plot. The proportion of craters with impact-related magnetic signatures when analyzing the real magnetic field models is seen to generally increase with increasing crater diameter. For the craters in the magnetized class, the fractions are about 4, 10, 13, and 47% for the respective diameter bins of 90–128, 128–206, 206–582, and 582–1321 km. The percentages of craters in the demagnetized class are somewhat lower for most bins, with respective values of about 2, 4, 12, and 19%. For both classes, the percentages of craters with magnetic signatures when using the synthetic magnetic field models are generally only a few percent (shown using transparent cross-hatching), but for some bins, the percentages can be higher.

In Fig. 5, we plot the average debiased percentages of craters with impact-related magnetized and demagnetized signatures for the three diameter ranges corresponding to complex craters (90–206 km), peak-ring basins (206–582 km), and multi-ring basins (582–1321 km). When only considering the certain and probable fidelity levels (plotted using dark shades), about 1%, 3%, and 14% of the complex craters, peak-ring basins, and multiring basins are found to have magnetized and demagnetized signatures, respectively. When considering all three signal fidelity levels (plotted using light shades), the results show the same trend of increasing percentage with increasing diameter, but the percentages are higher. In particular, craters with magnetized signatures are 3%, 5%, and 22% for the three respective diameter bins, whereas, for craters with demagnetized signatures, the corresponding percentages are 2%, 10%, and 19%.

In the right panels of Figs. 4 and 5, we plot the fractions of craters with impact-related magnetized and demagnetized signatures as a function of crater age. When considering only the certain and probable fidelity levels for the debiased results in Fig. 5, we see that about 2% and 3% of craters with pre-Nectarian and Nectarian ages show evidence of impact-related magnetic signatures, respectively. None of the younger Imbrian, Eratosthenian, or Copernican periods show evidence of craters with impact-related magnetized signatures for the highest two fidelity levels. When craters in the least reliable (possible) fidelity level are included, the percentages increase only modestly for the pre-Nectarian and Nectarian classes, but the percentage of craters in the Imbrian period increases to a value that is comparable to the older periods. This change for the Imbrian period, however, is based on only a single crater, Tsiolkovsky, that the two analysts both assigned the lowest signal fidelity level. In fact, the debiased number of craters in this group is less than 1. For this crater, we note that there is no central anomaly visible at 30 km altitude in either the Tsunakawa et al. (2015) or Hood et al. (2021b) magnetic field models. We further note that no

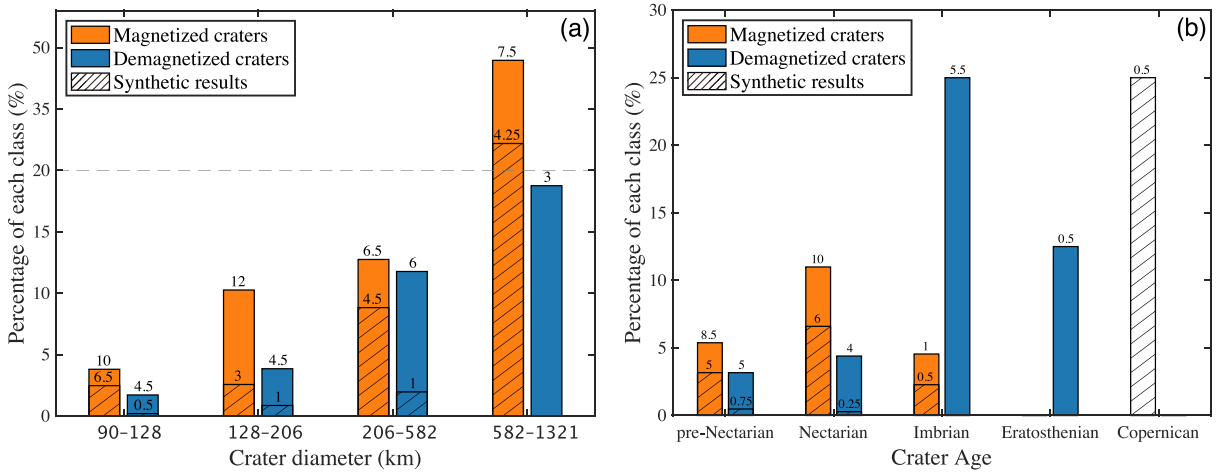

Fig. 4. Percentages of craters in the impact-related magnetized and demagnetized classes based on the surface magnetic field models as a function of (a) crater diameter and (b) age. Each plot considers craters that have diameters larger than 90 km, each bin corresponds to the average of the two analysts and transparent cross-hatching is used to denote the average result from the two synthetic magnetic field models. The number above each bar provides the average number of craters in the interval from the two analysts. The gray dashed line in Fig. 4a denotes a change in scale of the y axis.

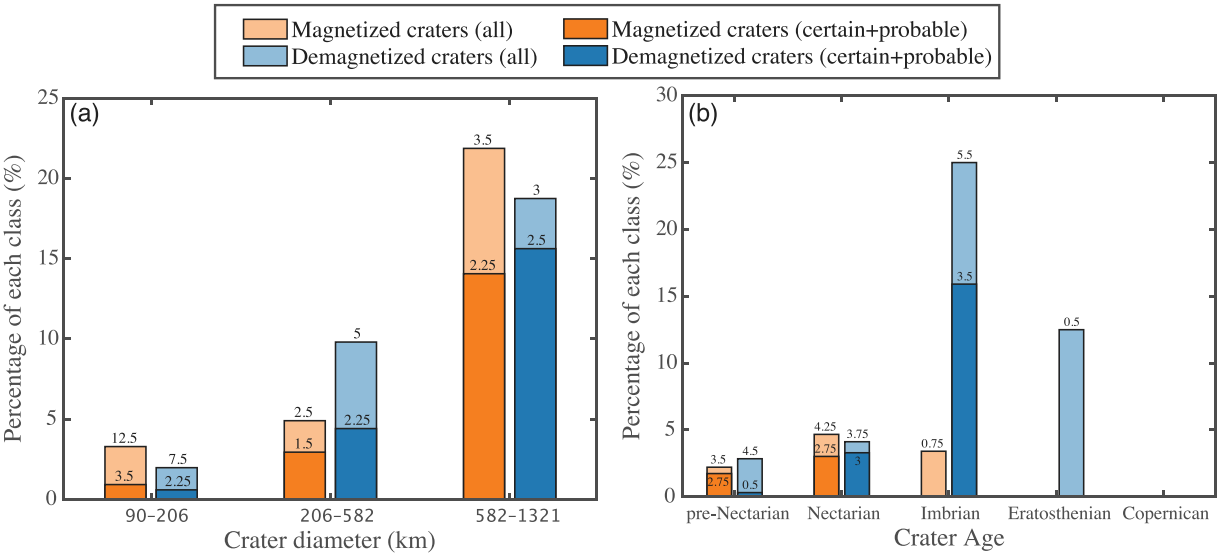

Fig. 5. Average debiased percentages of the two analysts for craters with impact-related magnetized and demagnetized signatures as a function of (a) crater diameter and (b) crater age using the surface magnetic field models. The number above each bar shows the average number of craters in the interval from the two analysts after debiasing. The light-colored bars show the results when all three signal fidelity levels are combined, whereas the dark-colored bars show the results when only certain and probable fidelity levels are used. We note that the absolute number of craters in each bin is not equal to the difference of the numbers using the real and synthetic magnetic field data in Fig. 4, as some negative numbers were set to 0 in the debiasing procedure (see Tables S1 and S2).

other studies have identified an impact-related magnetic anomaly with the Tsiolkovsky crater.

When considering the demagnetized class in Fig. 5 for craters with certain and probable signal fidelity levels, we find that about 0.3% and 3% of pre-Nectarian and Nectarian aged craters show evidence of impact-related demagnetization signatures, respectively (increasing to about 3% and 4% when all fidelity levels are used). The percentage of craters in the demagnetized class is considerably higher in the Imbrian period at about 16% for the highest two fidelity levels (increasing to 25% when all fidelity levels are included). We also find a high debiased percentage of craters in the demagnetized class for the Eratosthenian period, but this is based on only a single crater (Langrenus) that was assigned the lowest signal fidelity by only a single analyst. Similar to the crater Tsiolkovsky, we note that the number of debiased craters in this group is less than 1 and that there is no clear signal at 30 km altitude in either of the Tsunakawa et al. (2015) or Hood et al. (2021b) magnetic field models for this crater.

Two-dimensional plots of the debiased percentages as a function of both crater diameter and age can be found in Figure S4. The most remarkable aspect of these plots concerns the multi-ring basins. After debiasing, multi-ring basins with impact-related magnetized signatures are found only during the Nectarian period with an average percentage of 62.5% (3.75 in number). In contrast, all multiring basins in the Imbrian period have demagnetized signatures (2 in number), as do 25% of the pre-Nectarian basins (1 in number).

Finally, we note that we also performed the above analyses using the 30 km altitude magnetic field maps, with the results being shown in Figures S5–S7. For convenience, only a single synthetic magnetic field model was used in this analysis, as opposed to two when using the surface maps. The results from the 30 km maps are broadly similar to those presented above: (1) the percentage of magnetized and demagnetized craters increases with crater diameter, (2) debiased results show that magnetized craters are found only in the pre-Nectarian and Nectarian periods, but not for younger periods, and (3) the percentage

of demagnetized craters is highest in the Imbrian period. The main difference is that the number of craters identified as being impact demagnetized in the 30 km maps is considerably less than when using the surface maps. In particular, an average of only 3.5 demagnetized craters were identified by the two analysts in contrast to 18 when using the surface magnetic field maps. This difference is likely related to the weak demagnetization signatures being attenuated with altitude above the surface.

3.2. Spatial distribution of craters with magnetic signatures

We plot in Fig. 6 the locations of all craters with diameters greater than 90 km that were classified by at least one analyst as having an impact-related magnetic signature. When considering only those craters that both analysts agreed upon, of the 447 craters in our database with diameters greater than 90 km, 10 craters were classified as demagnetized and 30 as magnetized, which corresponds to about 9% of all craters having a magnetic signature. When including all craters that were classified as either magnetized or demagnetized by at least one analyst, the number of demagnetized craters increased to 26 and the number of magnetized craters increased to 42 (see Tables S3 and S4), which corresponds to a total of 15% of all craters having a potential magnetic signature.

The spatial distribution of craters in the magnetized and demagnetized classes are broadly similar. When considering craters with $D \leq$ 582 km (complex craters and peak-ring basins), there is an absence of craters with magnetized and demagnetized signatures in the prominent magnetic lows that correspond to the Procellarum KREEP Terrane and the northern farside highlands (see Wieczorek, 2018b; Wieczorek et al., 2022). These magnetic lows are most visible when plotting the field strengths using a logarithmic color scale. Because of this, there are more craters with magnetic signatures in the southern hemisphere than in the northern hemisphere. In contrast to the complex craters and peak-ring basins, 7 of the multi-ring basins with magnetic signatures are located on the nearside with only 4 on the farside. In total, about two-thirds of the impact craters with magnetic signatures are located on the farside. Of those craters that are located on the farside, about 60% are found close to the strong regional magnetic highs, with others being found far from these regions.

The distribution of craters with impact-related magnetic signatures is shown in Figure S8 based on the 30 km altitude magnetic field maps. In contrast to the 42 and 26 craters that were classified as having a magnetized or demagnetized signature by at least one analyst with the surface data, we find respectively only 35 and 5 with the 30 km altitude maps. Regarding those craters that were classified differently, in most cases, craters that were classified as having an impact-related magnetic signature in the surface maps were classified as having no signal in the 30 km maps. Nevertheless, in a small number of cases, craters were classified as having a magnetic signature in the 30 km maps but not in the surface data. For craters with magnetized signatures, these include Moscoviense, Moscoviense North, Hirayama, Repsold, Mitra, Rosenberger, and five unnamed craters. For craters with demagnetized signatures, these include Freundlich-Sharonov, Engel'gardt B, and Inghirami.

3.3. Crater magnetic field profiles

Halekas et al. (2002, 2003) previously investigated the magnetic signatures of lunar craters and basins using azimuthally averaged surface magnetic field strengths derived from electron reflectometry. In contrast to these previous studies, our results are instead based on global vector magnetometer measurements. Here we calculate the azimuthally averaged radial profiles of all craters that were classified as having an impact-related magnetic signature by at least one of the analysts in Fig. 6, of which there are 68. In constructing these profiles, we collected all pixels in the magnetic field intensity map that were between two different radii from the center of the crater. The average value in this annulus was then computed after weighting the individual values by the pixel area on the surface of the Moon. The radii of the annuli were chosen so that their midpoints were separated by 0.2 crater radii. This led to having 6 measurements as a function of radial distance within the crater rim, which is sufficient to quantify the profiles for this study. Though electron reflectometry provides a more direct measurement of the field strength at the surface than does orbital magnetometry-based methods, our azimuthal averaging of the surface magnetic field strength data should minimize any noise that is present in the magnetometer-based models.

Similar to Halekas et al. (2002), we divided the craters into two groups based on the intensity of the surrounding regional magnetic fields at distances of 3–4 crater radii. If the average field strength of the surroundings was greater than 10 nT, the crater was considered to be located in a region of strong magnetic fields, whereas for values less than this the crater was classified as being in a region of weak magnetic fields. In total, 13 craters with magnetized signatures and 15 craters with demagnetized signatures are located in regions with strong magnetic fields, and 29 craters with magnetized signatures and 11 craters with demagnetized signatures are located in regions of weak magnetic fields. No clear trend was found in the magnetic field intensity profiles as a function of crater diameter or age in this study. Thus, to facilitate the comparison of the profiles, we normalized the distance by the crater radius. Given that the strength of the crater magnetic anomalies varies greatly, two different approaches were used to normalize the magnetic field intensity measurements. In the first approach (normalized), the field strength was divided by the average field strength of the surroundings between 3 and 4 crater radii, whereas for the second approach (relative), the average field strength of the surroundings was subtracted from the magnetic field profile.

For craters in the magnetized class, Fig. 7 shows that the magnetic highs are located entirely within the crater rim. The intensities of the central magnetic highs are on average about two times the background field strength with a maximum enhancement of a factor of about seven (Fig. 7a,b). The magnetic signatures are most clear for those craters that formed in regions with weak magnetic fields. For those that formed in regions with strong magnetic fields, the profiles have much more variability, and for a few craters, the central magnetic highs are weaker than the surrounding background field, explaining why some profiles appear to have relatively low values in their interior. The central magnetic highs of the craters that formed in regions with weak magnetic fields are about 5 nT larger than the surroundings on average, with 6 of them stronger than 8 nT (Fig. 7c). Most of the craters that formed in the regions with strong magnetic fields have a central anomaly high that is stronger than 10 nT with respect to the surroundings, with an average value of about 33 nT (Fig. 7d).

The magnetic lows of craters with impact-related demagnetized signatures extend outwards on average to about 1.5 crater radii. For craters that formed in regions with weak magnetic fields, the magnetic lows usually extend beyond the crater rim, with some extending up to 3–4 crater radii (Figs. 7e,g). The magnetic field strength is reduced on average by a factor of about two, and the central magnetic low of the average profile is about 3 nT less than the surrounding terrains. For craters that formed in regions of strong magnetic fields (Figs. 7f,h), the demagnetization signature is usually located entirely within the crater rim. The reduction in field strength is on average just under a factor of two, and the field strengths are about 10 nT weaker than the surroundings.

4. Discussion

4.1. Lunar dynamo history from magnetized and demagnetized craters

We have made use of modern magnetic field models and crater databases to classify the magnetic signatures of lunar impact craters.

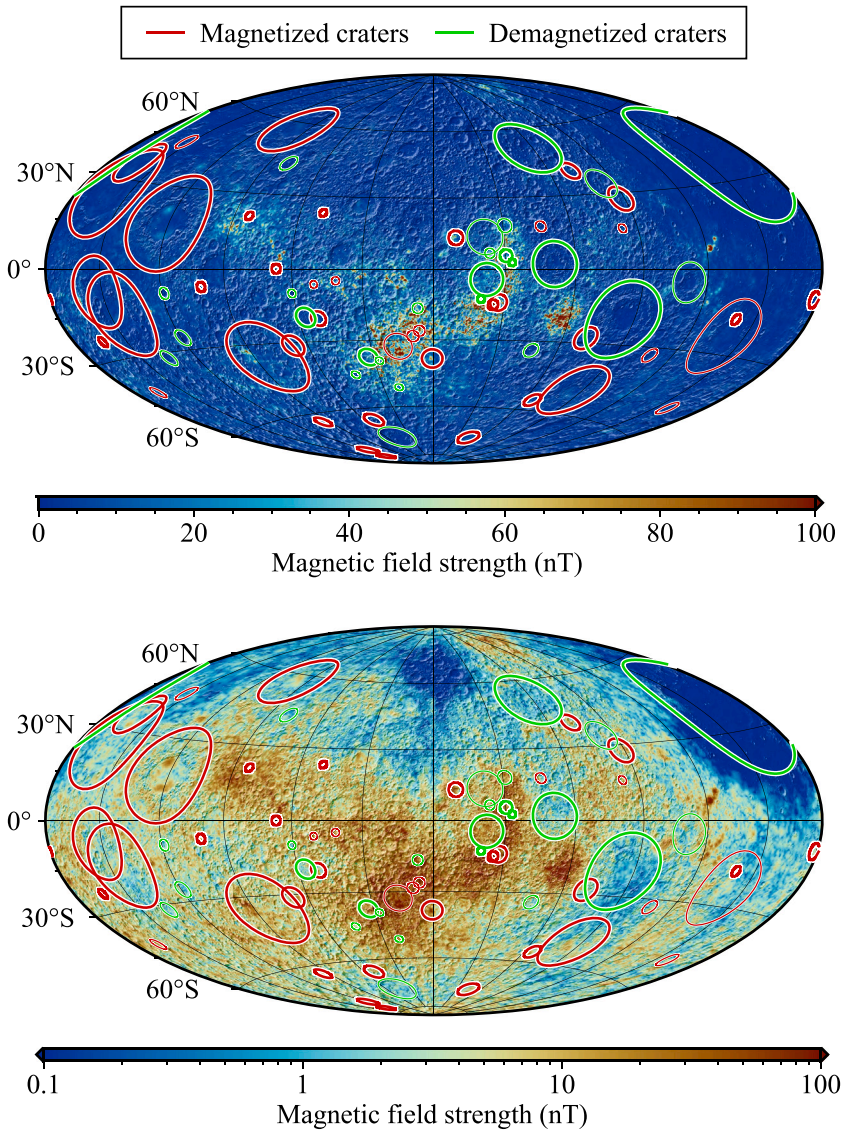

Fig. 6. The spatial distribution of craters in the magnetized (red) and demagnetized (green) classes superposed on the total magnetic field strength at the surface plotted using linear (upper) and logarithmic (lower) scales. Bold circles denote the main rims of those craters that were classified the same by both analysts, whereas the thin circles represent those craters that were classified as either magnetized or demagnetized by only a single analyst. The surface magnetic field strength from the model of Tsunakawa et al. (2015) is plotted using a Mollweide equal-area projection, centered on the farside at 180° E. The maximum value of the magnetic field strength is about 718 nT and the color scale is saturated beyond 100 nT. (For interpretation of the references to color in this figure legend, the reader is referred to the web version of this article.)

Only 68 out of 447 craters (about 15%) with diameters greater than 90 km were classified to have an impact-related magnetized or demagnetized signature by at least one analyst. This is comparable to the previous study of Arkani-Hamed and Boutin (2014) who found 58 craters with diameters greater than 100 km with magnetic signatures. In contrast, Halekas et al. (2002) found 100 craters with demagnetized signatures with diameters greater than 50 km using Lunar Prospector electron reflectometer data. The larger number of demagnetized craters in Halekas et al. (2002) compared to our results is at least partially a result of them having considered slightly smaller craters that are more numerous, but it is also possible that the electron reflectometer data might be better suited than the orbital magnetometer data when investigating weak surface field strengths.

Halekas et al. (2003) showed that the magnetic signatures of lunar impact basins with diameters greater than 300 km are correlated with their ages: Imbrian basins display magnetic lows inside the basin rim, many Nectarian basins have central magnetic highs, and the pre-Nectarian basins are more ambiguous and do not show clearly distinguishable magnetic signatures. Such observations were further confirmed by later studies that made use of orbital magnetometer measurements (e.g., Hood, 2011; Le Bars et al., 2011; Oliveira et al., 2017). The magnetic signatures of the craters in our study, many of which are considerably smaller than 300 km, are generally compatible with these observations.

Our debiased results show that the fraction of craters with impact-related central magnetic highs is about 2%–3% during both the pre-Nectarian and Nectarian periods when only certain and probable fidelity levels are considered (which corresponds to a total of about 5 craters on average). Less than one crater in the Imbrian period was classified as being magnetized on average, but the corresponding crater was also classified as having the lowest signal fidelity level, and as discussed in Section 3, we do not rely on this crater to draw any conclusions. After debiasing, we find no evidence for craters with impact-related central magnetic highs in the Eratosthenian or Copernican periods. The ages of the craters in the magnetized class thus suggest that a strong ambient magnetic field was present for at least portions of the pre-Nectarian and Nectarian periods. The lack of convincing central magnetic anomalies in the younger periods is consistent with either a

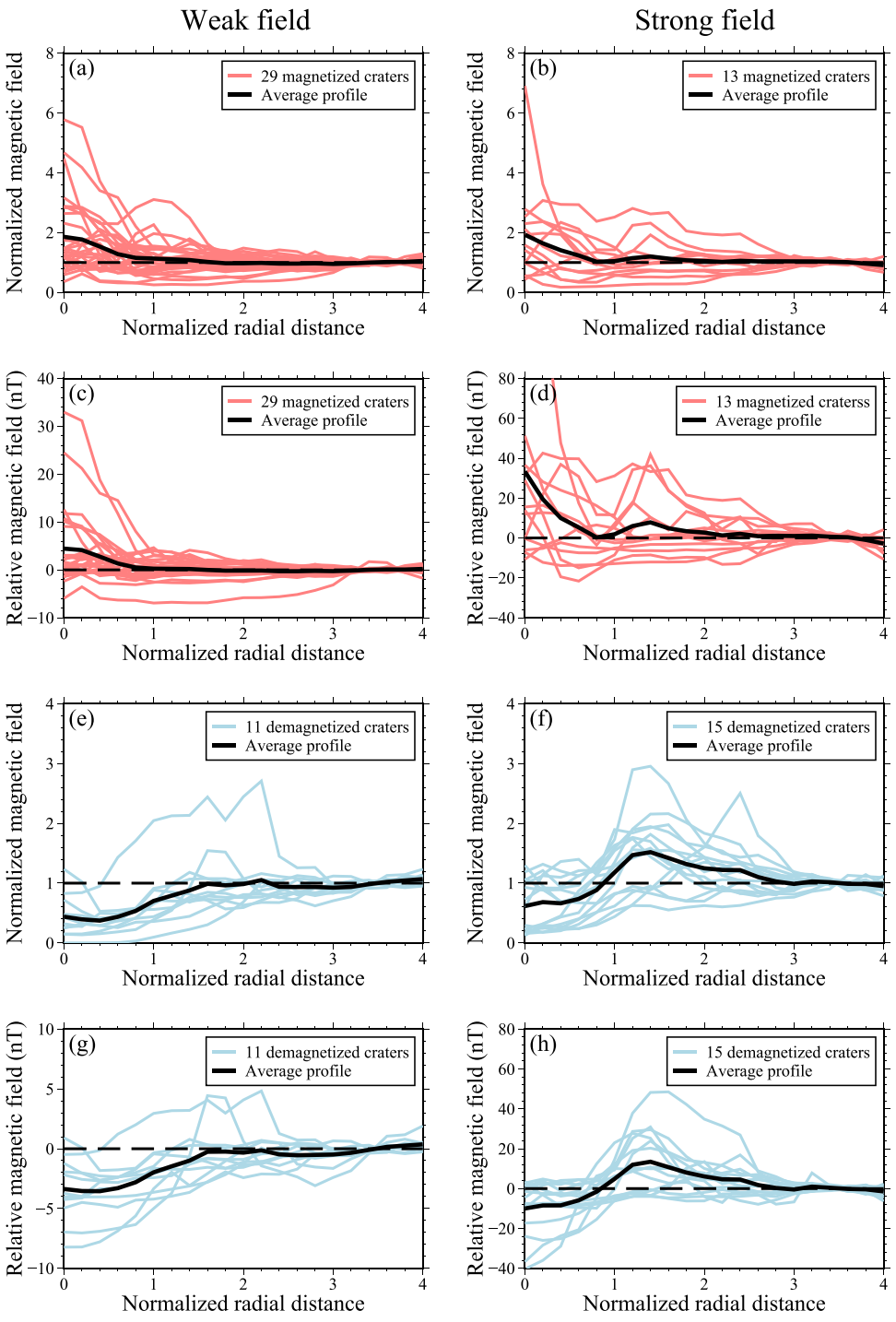

Fig. 7. Azimuthally averaged magnetic field intensity profiles of the craters shown in Fig. 6 as a function of distance from the crater center. The left column plots profiles for those craters located in regions with weak magnetic fields, whereas the right column is for craters located in regions with strong magnetic fields. The profiles are either normalized by the average field strength (a,b,e,f) or are relative to the average field strength (c,d,f,h) as defined by the average value within 3–4 crater radii. The red lines represent the craters in the magnetized class, the blue lines represent the craters in the demagnetized class, the black lines represent the average of the profiles, and the back dashed lines represent the background field. The radial distances are normalized by the crater radius. (For interpretation of the references to color in this figure legend, the reader is referred to the web version of this article.)

weak dynamo field during these periods or the absence of a dynamo altogether. Our debiased fraction of craters in the demagnetized class is about 0.3%–3% in the pre-Nectarian and Nectarian periods when only the certain and probable fidelity levels are used (which corresponds to a total of about 3.5 craters) and dramatically increases to about 16% in the Imbrian period (which corresponds to about an average number of 3.5). These observations suggest that there was not a strong field present during much of the Imbrian period. We caution that the total number of Eratosthenian and Copernican craters in our analysis is small (there are only 6 craters with $D > 90$ km), and that this hinders drawing any definitive conclusions for these two youngest time periods.

The number of craters with impact-related magnetized and demagnetized signatures in the pre-Nectarian and Nectarian periods is comparable. This observation could be accounted for either by a dynamo that was operating intermittently or (as discussed in Sections 4.2 and 4.3) by the requirement of special impact conditions to produce

a magnetic anomaly. Regardless, the age distributions of craters in both the magnetized and demagnetized classes suggest that strong fields were present during at least portions of the pre-Nectarian and Nectarian periods and that the surface magnetic field strength was substantially weaker or absent during much of the Imbrian and later periods. We acknowledge that some impact crater demagnetization signatures could perhaps have become obscured over time by other geological processes (see Halekas et al., 2002). Nevertheless, even if the number of craters with demagnetization signatures was larger than what we find for the oldest geologic periods, this would not modify our inferences regarding the temporal evolution of the dynamo field.

Our results are broadly compatible with lunar paleomagnetic analyses that imply strong fields in the distant past and weak fields at younger times. However, the predicted transition times between the weak and strong field epochs of the paleomagnetic and impact crater approaches are not entirely consistent. The paleomagnetic analyses suggest that the lunar dynamo had Earth-like field strengths from about 4.2 Ga in the pre-Nectarian and Necatarian periods to at least 3.56 Ga in the Imbrian period (Tikoo et al., 2014). The field strength then decreased by an order of magnitude at some point between 3.56 and 3.2 Ga and the dynamo ceased altogether at some point between ~1.92 and ~0.8 Ga (Mighani et al., 2020). The younger bound for the transition from strong to weak fields corresponds approximately to the boundary of the Imbrian and Eratosthenian periods, which is commonly quoted as having the same age of 3.2 Ga (e.g., Stöffler et al., 2006). The upper bound for this transition is about halfway through the Imbrian period, with the Nectarian-Imbrian boundary being dated to 3.85 Ga (e.g., Stöffler et al., 2006). Our crater magnetization results, however, provide little evidence for strong magnetic fields at any point during the Imbrian period.

Eight craters were classified by at least one analyst to have an impact-related demagnetization signature in the Imbrian period. Both analysts classified the two Imbrian-aged multiring basins (Imbrium and Orientale) as being demagnetized. The Imbrium basin (which defines the beginning of the Imbrian period) is dated to have formed at 3.85 Ga, and crater counting studies estimate that the Orientale basin formed at about 3.73 Ga (e.g., Le Feuvre and Wieczorek, 2011). The Schrödinger and Petavius craters were each classified as demagnetized by one analyst, and they are known to have formed in time between the Imbrium and Orientale basins (e.g., Wilhelms et al., 1987; Fassett et al., 2012). Four of the eight Imbrian-aged craters with potential demagnetization signatures thus formed during the high-field strength epoch as defined by the paleomagnetism results. We are not aware of any age estimates for the other four craters, but it is probable that some of these formed before 3.56 Ga as well. During the Imbrian period, the impact flux transitioned from being exponential in time to linear in time. Because of this, the Neukum et al. (2001) chronology function predicts that about 86% of the Imbrian-aged craters would have formed between 3.85 and 3.56 Ga, with the remaining 14% forming between 3.56 and 3.2 Ga. With 22 Imbrian-aged craters in our study, only about 3 should have formed after 3.56 Ga. Thus, one or more of the four undated craters could also have formed before 3.56 Ga.

We note that Hood et al. (2021b) argued that some elongated magnetic anomalies on the lunar nearside could be the result of ejecta derived from the Imbrium and Orientale impact basins. If true, this would imply the existence of strong surface fields at the time these basins formed in the early Imbrian period. Nevertheless, the association between these two basins and the elongated magnetic anomalies is equivocal: they could be related to other older impact basins, or have a non-impact origin altogether. In fact, it has been shown that the Fra Mauro formation, which represents ejecta from the Imbrium basin, is on average associated with weaker surface field strengths than the nearside highlands (Halekas et al., 2001). We also note that Kelley and Garrick-Bethell (2020) quoted an upper bound of ~3.9 Ga for the age of the Reiner Gamma magnetic anomaly based on the interpretation that part of it formed within an ancient impact crater. Though the suggested age of ~3.9 Ga for the pre-impact basaltic basement materials is plausible, older volcanic materials do exist on the Moon, and thermal evolution models show that nearside volcanism could have occurred throughout the pre-Nectarian and Nectarian periods (e.g., Laneuville et al., 2018).

The discrepancy in the age of the transition from high to low dynamo field strengths based on the impact crater and paleomagnetism approaches (as previously noted by Halekas et al., 2003) is disconcerting. It is particularly troublesome because almost all of the paleomagnetic analyses that predict high field strengths are for rocks that formed in the Imbrian period, with ages between about 3.85 and 3.56 Ga (e.g., Weiss and Tikoo, 2014). Three explanations for this discrepancy are possible. First, it is possible that the small number of paleomagnetic analyses and/or the small number of Imbrian-aged impact craters are insufficient to accurately assess the time evolution of the dynamo field during this important time in lunar evolution. Second, it is possible that some of the Imbrian-aged craters could have central magnetic highs, but that they are too weak to be detected in the orbital magnetic field datasets. Lastly, it is possible that the high Earth-like paleomagnetic field strengths reported for the early Imbrian period might need to be revised. In particular, we note that all of the reported Earth-like paleomagnetic field strengths used isothermal demagnetization techniques. The few paleomagnetic analyses that were conducted on lunar rocks using more accurate thermal demagnetization techniques, however, all obtained field strengths that were significantly lower (Tikoo et al., 2017; Mighani et al., 2020; Tarduno et al., 2021).

Lastly, we remark that even though about 15% of the craters we analyzed show evidence for either impact-related magnetization or demagnetization, the vast majority of craters in our study (about 85%) have no apparent magnetic signature at all. There are several factors that could contribute to explaining this observation. First, as suggested above, it is possible that the lunar dynamo was episodic. This could potentially account for the similar number of craters in the magnetized and demagnetized classes in the pre-Nectarian and Nectarian periods, with the other craters forming when the field was changing and unstable. An episodic dynamo could also perhaps explain contradictory paleomagnetism results during the Imbrian and younger periods (see Tarduno et al., 2021). Second, it is possible that the dynamo was reversing or changing direction on timescales comparable to the cooling timescales of impact melt sheets (see Oliveira and Wieczorek, 2017; Takahashi and Tsunakawa, 2009). Such a directionally unstable dynamo would give rise to a smaller net remanent magnetization interior to the crater. Lastly, it is possible that only a small fraction of impact events have the required conditions to generate a magnetic signal at spacecraft altitudes. For example, the generation of detectable magnetic signatures could require specific impact velocities (Cintala and Grieve, 1998), impact angles (Pierazzo and Melosh, 2000; Zhu et al., 2019), or iron-metal contents of the impactors (Oliveira et al., 2017). In the following subsections, we discuss the mechanisms that could account for the magnetized and demagnetized signatures that we observe.

4.2. Demagnetization mechanisms

The craters with impact-related demagnetized signatures in our study have a central magnetic low that extends from the crater center to at least the crater rim. In some cases, the demagnetization signature extends up to 4 crater radii from the center, especially for those craters that formed in regions with weak magnetic fields. Compared to the surroundings, the magnetic field strengths are reduced by a factor of about two on average, but there is considerable variability in the magnitude of the reduction. Three mechanisms related to an impact event could contribute to accounting for these reductions in magnetic field strength: crustal excavation, thermal demagnetization, and shock demagnetization.

The excavation of crustal materials during crater formation could remove previously magnetized materials inside of the crater rim and

would act to randomize the directions of magnetization in the ejecta that is deposited outside of the crater. The maximum depth of excavation of materials with respect to the pre-impact surface is about one-tenth the crater diameter (Melosh, 1989), and for the craters in our study (90–1321 km), this corresponds to excavation depths ranging from about 9 to 132 km. These depths represent a considerable fraction of the total crustal thickness, which on average is about 34 to 43 km (Wieczorek et al., 2013). Thus, excavation of previously magnetized crust could contribute to the magnetic lows found in many craters.

If excavation was the main contributor to the demagnetization signatures, then one might expect to see a size-dependent demagnetization signature. Whereas the smallest craters would only excavate a fraction of the magnetized crust, the largest craters would have excavated the entire magnetized crust. Consistent with Halekas et al. (2002), however, we did not find any trend in the demagnetization signature as a function of crater size. Halekas et al. (2002) interpreted the lack of a size dependence on the crater demagnetization signature as indicating that all the craters in their investigation ($D > 50$ km) completely penetrated the magnetic layers. For our study, the maximum depth of excavation of the smallest crater investigated is about 9 km. If excavation was the only process that demagnetized the crust, this would imply that the pre-existing magnetization in the crust should be confined to the upper 10 km.

The crustal materials close to the impact site experience high temperatures that can exceed the Curie temperature. If there was no dynamo field present at the time the crater formed, these thermally demagnetized materials would not acquire any new magnetization as they cooled through the Curie temperature. The extent of the crust that experiences temperatures above the Curie temperature has not, to our knowledge, been calculated, though it could easily be done using a shock physics code such as iSALE (Collins et al., 2004; Wünnemann et al., 2006). Nevertheless, we can use the distribution of impact melt in a crater as a proxy for those regions that experienced high temperatures. The thickest deposits of impact melt are usually located within the crater rim and within the peak ring for larger craters (Cintala and Grieve, 1998). Thus, thermal demagnetization could likely account for the demagnetization signature within the crater rim (or peak ring), but not exterior to the crater rim.

The passage of an impact-generated shock wave is another process that could demagnetize the crust if there was no dynamo field present when the impact occurred. Previous studies have shown that an impact shock wave could demagnetize the magnetic materials within a few crater radii of the impact point (Halekas et al., 2002, 2003; Mohit and Arkani-Hamed, 2004). Using the scaling laws that were summarized in Melosh (1989), for a vertical impact with a velocity of 17 km/s that would form a 90 km crater, the peak hemispherical shock pressure decays to 1 GPa at about one crater radius and further decays to 0.1 GPa at about 3 crater radii. Experiments suggest that magnetic materials should lose their initial magnetization at a pressure of about 1 GPa (Bezaeva et al., 2007, 2010), and this could account for any demagnetization within the crater rim. Given that the average thickness of the lunar crust is somewhere between 34 and 43 km (Wieczorek et al., 2013), the hemispherical shock wave generated by a 90-km-diameter crater or larger would demagnetize the entire lunar crust within the crater rim if there was no dynamo field present. Because of this, we would not expect to see any size dependence in the demagnetization signature for the craters in our study.

We note that the demagnetization signatures of craters that formed in regions with weak and strong magnetic field strengths are somewhat different. For those that formed in regions with strong ambient field strengths, the magnetic lows extend to the crater rim, whereas in the regions with weak fields, the magnetic lows can extend up to 4 crater radii. The excavation of crustal materials and thermal demagnetization should not affect the pre-existing crustal magnetization exterior of the crater rim. Thus, shock demagnetization is the most likely explanation for any demagnetization that occurs exterior of the crater. Why this shock demagnetization signature is more visible in regions of low magnetic field strengths than high is not clear.

4.3. Magnetization mechanisms

Craters with impact-related magnetized signatures in this study have a central magnetic high that is entirely confined to the interior of the crater rim. In some cases, this magnetic high is surrounded by a magnetic low that extends to the crater rim. The field strengths of the magnetic highs range from a few to a few tens of nT. The magnetic field strengths in the crater centers are about two times larger than the surroundings on average, but they also show a large variation in the field magnitude ranging up to a maximum factor of about seven. If an impact occurred in the presence of a dynamo field, the materials within the crater could acquire a remanent magnetization by two processes: shock remanence and thermal remanence.

If a dynamo field was present when an impact occurred, the passage of the shock wave could have magnetized portions of the crust by the process of shock remanent magnetization. Shock-remanent magnetization is about a factor of three to five times less efficient than thermal magnetization (Gattacceca et al., 2008), but it can affect nearly all the crust within the crater rim (see Section 4.2). Shock-remanent magnetization, however, is unlikely to be the main contributor to the central magnetic highs found in the craters of this study. The central magnetic high usually encompasses only a fraction of the crater interior (as seen in Fig. 2), whereas the shock wave should be capable of magnetizing materials to the crater rim.

Thermal remanence is the most plausible origin for the central magnetic anomalies found in lunar impact craters and basins. The largest quantities of impact melt are expected to concentrate in the central portion of the crater, or within the peak ring for larger craters (Cintala and Grieve, 1998). Though indigenous lunar rocks are metal-poor and might not acquire a sufficiently strong magnetic remanence to be observed from orbit, iron metal delivered by the projectile can make the impact melt of a crater many times more magnetic. Modeling by Oliveira et al. (2017) showed that the central magnetic highs associated with lunar impact basins could plausibly be a result of small quantities of such metallic iron (0.1–0.5 wt%) being present in the central impact melt sheet. A possible explanation as to why some craters of the same age show evidence for crustal magnetization, whereas others do not, could simply be a result of the variable amounts of projectile materials that are retained within the impact crater. The abundance of projectile iron metal within the crater would depend upon not only the composition of the projectile but also the impact angle of the event (Wieczorek et al., 2012; Zhu et al., 2019).

We estimate the magnetic field strength generated by a magnetized impact melt sheet to see if it could account for the observations. The impact melt is assumed to be uniformly magnetized, the direction of magnetization is assumed to be vertical, its geometry is assumed to be a single spherical prism with a radius of 0.5 crater radii, and the volume of impact melt is taken from Eqs 6 and 8 in Cintala and Grieve (1998), which depends on crater diameter with a power of 3.26. We further assume that the magnetization of the impact melt is 0.1 Am^{-1}, which corresponds to the minimum value estimated for the Nectarian basins by Oliveira et al. (2017) and which is consistent with the magnetizations expected for lunar impact melt breccias (Wieczorek et al., 2012).

The maximum magnetic field strength of a 90 km diameter crater is estimated to be about 4 nT, whereas, for the largest peak-ring basin with a diameter of about 600 km, the maximum field strength is about 30 nT. These estimated field strengths are comparable to those found in the craters of our study that generally are a few to a few tens of nT (see Fig. 7). This observation suggests that thermal remanent magnetization in the impact melt sheet is capable of explaining the observed central magnetic highs of the craters in our study. Given that the amount of impact melt that is generated decreases exponentially with decreasing crater size, we would not expect to detect this magnetic signature in craters smaller than about 90 km, which is also in good agreement with our observations.

Finally, we note that lateral variations in the abundance of metallic iron in the lunar crust could also contribute to the magnitude of the central magnetic high found in some impact craters. If metallic iron existed in the crust before the impact, this would be added to the amount of metal brought by the impactor. Fig. 6 shows that there is a clear dearth of craters with impact-related magnetized signatures in the regional magnetic lows near the Procellarum KREEP Terrane and northern farside highlands. One possible explanation for this observation is that the crust in these regions could have a lower abundance of metallic iron than elsewhere on the Moon.

5. Conclusions

In this study, we investigated the impact-related magnetic signatures of lunar craters using modern magnetic field models and crater databases. Craters with diameters between 90 and 1321 km were divided into three classes: magnetized, demagnetized, and no signal. A signal fidelity level was assigned to each of the craters with a magnetic signature, and synthetic magnetic field models were used to estimate the number of false identifications in each class. To avoid further bias, two analysts conducted the classifications independently. The classifications were then used to constrain the lunar dynamo history and the origin of crater magnetic signatures.

In total, about 15% of craters with diameters greater than 90 km (68 in number) were classified as having impact-related magnetized or demagnetized signatures by at least one of the analysts. After debiasing, about 13% of peak-ring and multi-ring basins ($D > 206$ km) present a magnetic signature on average, whereas smaller craters are rarely associated with magnetic signatures (about 1.5% on average). In terms of crater age, craters in both the magnetized and demagnetized classes are found in the pre-Nectarian and Nectarian periods, but there is little evidence for craters with impact-related magnetized signatures in the younger Imbrian, Eratosthenian, and Copernican periods. The proportion of craters with demagnetized signatures is also significantly higher in the Imbrian period than in the older pre-Nectarian and Nectarian periods. These results are compatible with a lunar dynamo operating during at least portions of the pre-Nectarian and Nectarian periods, and with the dynamo field either weakening or ceasing at the beginning of the Imbrian period. Whereas paleomagnetic analyses suggest that a strong dynamo field was present from about 4.2 Ga to at least 3.56 Ga halfway through the Imbrian period, our results based on impact crater magnetization imply that the transition from strong to weak fields occurred near the Nectarian-Imbrian boundary at 3.85 Ga.

One of the surprising outcomes of our study is that the vast majority of lunar craters (about 85%) were found not to have any impact-related magnetic signature at all. The small number of craters with magnetic signatures could potentially be a result of an episodic dynamo, a dynamo that was frequently reversing, or a dynamo that was unstable in intensity and direction. Alternatively, specific impact conditions could perhaps be required to generate a magnetic signature, of which the most important are probably the impact angle and the iron-metal content of the impacting projectile.

Lastly, our results place constraints on the mechanisms that are responsible for generating the magnetized or demagnetized signatures of lunar impact craters. Demagnetization signatures generally extend to the crater rim, and sometimes up to 4 crater radii. Excavation of magnetic materials and the thermal demagnetization of the crust can account for magnetic lows within the crater rim. Shock demagnetization can potentially account for demagnetization that extends beyond the crater rim, but only if there was no ambient magnetic field present when the crater formed. In contrast, the central magnetic highs associated with some craters are likely to be a result of impact melt that cooled in the presence of a dynamo field. Since the amount of impact melt that is generated decreases with crater size, craters smaller than about 90 km in diameter will have weak signatures that will be difficult to detect from orbit using the current magnetometer data sets.

CRediT authorship contribution statement

Xi Yang: Writing – review & editing, Writing – original draft, Visualization, Software, Methodology, Data curation. **Mark Wieczorek:** Writing – review & editing, Supervision, Software, Methodology, Conceptualization.

Declaration of competing interest

The authors declare that they have no known competing financial interests or personal relationships that could have appeared to influence the work reported in this paper.

Data availability

The LOLA DEMs are archived at the NASA Planetary Data System (Neumann, 2009). The spherical harmonic coefficients of the two magnetic field models that were employed in this work can be downloaded at Wieczorek (2018a) and Ravat et al. (2020b). The impact crater database of Robbins (2019) can be downloaded at Robbins (2018). The "Lunar Impact Crater Database (2015)" can be downloaded at Losiak et al. (2015). The complete database of lunar crater magnetic signature classifications, the derived magnetic field profile data, and the figures that were used to classify the crater magnetic signatures in this study can be accessed at Yang and Wieczorek (2024).

Acknowledgments

We thank Laurent Montesi and four anonymous reviewers for providing constructive comments that helped improve a prior version of this manuscript. We thank two additional anonymous reviewers for comments that helped improve the final manuscript. We also thank Dr. Teemu Öhman for discussions related to the LPI crater database that was used in this analysis. We gratefully acknowledge Dr. Wenzhe Fa for promoting the initial stages of this research project and for providing initial funding support. Mark Wieczorek acknowledges funding support from the French Space Agency, CNES.

Appendix A. Supplementary data

Supplementary material related to this article can be found online at https://doi.org/10.1016/j.icarus.2024.116049.

References

Arkani-Hamed, J., Boutin, D., 2014. Analysis of isolated magnetic anomalies and magnetic signatures of impact craters: Evidence for a core dynamo in the early history of the Moon. Icarus 237, 262–277. http://dx.doi.org/10.1016/j.icarus.2014.04.046.

Bezaeva, N.S., Gattacceca, J., Rochette, P., Sadykov, R.A., Trukhin, V.I., 2010. Demagnetization of terrestrial and extraterrestrial rocks under hydrostatic pressure up to 1.2 GPa. Phys. Earth Planet. Inter. 179 (1–2), 7–20. http://dx.doi.org/10.1016/j.pepi.2010.01.004.

Bezaeva, N.S., Rochette, P., Gattacceca, J., Sadykov, R.A., Trukhin, V.I., 2007. Pressure demagnetization of the Martian crust: Ground truth from SNC meteorites. Geophys. Res. Lett. 34 (23), http://dx.doi.org/10.1029/2007GL031501.

Binder, A.B., 1998. Lunar prospector: overview. Science 281 (5382), 1475–1476. http://dx.doi.org/10.1126/science.281.5382.1475.

Cébron, D., Laguerre, R., Noir, J., Schaeffer, N., 2019. Precessing spherical shells: flows, dissipation, dynamo and the lunar core. Geophys. J. Int. 219 (Supplement_1), S34–S57. http://dx.doi.org/10.48550/arXiv.1809.05330.

Cintala, M.J., Grieve, R.A., 1998. Scaling impact melting and crater dimensions: Implications for the lunar cratering record. Meteorit. Planet. Sci. 33 (4), 889–912. http://dx.doi.org/10.1111/j.1945-5100.1998.tb01695.x.

Collins, G.S., Melosh, H.J., Ivanov, B.A., 2004. Modeling damage and deformation in impact simulations. Meteorit. Planet. Sci. 39 (2), 217–231. http://dx.doi.org/10.1111/j.1945-5100.2004.tb00337.x.

Crameri, F., Shephard, G.E., Heron, P.J., 2020. The misuse of colour in science communication. Nat. Commun. 11 (1), 1–10. http://dx.doi.org/10.1038/s41467-020-19160-7.

Dwyer, C., Stevenson, D., Nimmo, F., 2011. A long-lived lunar dynamo driven by continuous mechanical stirring. Nature 479 (7372), 212–214. http://dx.doi.org/10.1038/nature10564.

Dyal, P., Parkin, C.W., Daily, W.D., 1974. Magnetism and the interior of the Moon. Rev. Geophys. 12 (4), 568–591. http://dx.doi.org/10.1029/RG012i004p00568.

Evans, A.J., Tikoo, S.M., 2022. An episodic high-intensity lunar core dynamo. Nat. Astron. 6 (3), 325–330. http://dx.doi.org/10.1038/s41550-021-01574-y.

Evans, A.J., Tikoo, S.M., Andrews-Hanna, J.C., 2018. The case against an early lunar dynamo powered by core convection. Geophys. Res. Lett. 45 (1), 98–107. http://dx.doi.org/10.1002/2017GL075441, URL https://onlinelibrary.wiley.com/doi/10.1002/2017GL075441.

Evans, A.J., Zuber, M.T., Weiss, B.P., Tikoo, S.M., 2014. A wet, heterogeneous lunar interior: Lower mantle and core dynamo evolution. J. Geophys. Res. 119 (5), 1061–1077. http://dx.doi.org/10.1002/2013JE004494.

Fassett, C.I., Head, J.W., Kadish, S.J., Mazarico, E., Neumann, G.A., Smith, D.E., Zuber, M.T., 2012. Lunar impact basins: Stratigraphy, sequence and ages from superposed impact crater populations measured from Lunar Orbiter Laser Altimeter (LOLA) data. J. Geophys. Res. 117 (E12), E00H06. http://dx.doi.org/10.1029/2011JE003951.

Garrick-Bethell, I., Weiss, B.P., Shuster, D.L., Buz, J., 2009. Early lunar magnetism. Science 323 (5912), 356–359. http://dx.doi.org/10.1126/science.1166804.

Garrick-Bethell, I., Weiss, B.P., Shuster, D.L., Tikoo, S.M., Tremblay, M.M., 2017. Further evidence for early lunar magnetism from troctolite 76535. J. Geophys. Res. 122 (1), 76–93. http://dx.doi.org/10.1002/2016JE005154.

Gattacceca, J., Berthe, L., Boustie, M., Vadeboin, F., Rochette, P., De Resseguier, T., 2008. On the efficiency of shock magnetization processes. Phys. Earth Planet. Inter. 166 (1–2), 1–10. http://dx.doi.org/10.1016/j.pepi.2007.09.005.

Gattacceca, J., Boustie, M., Lima, E., Weiss, B., De Resseguier, T., Cuq-Lelandais, J., 2010. Unraveling the simultaneous shock magnetization and demagnetization of rocks. Phys. Earth Planet. Inter. 182 (1–2), 42–49. http://dx.doi.org/10.1016/j.pepi.2010.06.009.

Gong, S., Wieczorek, M.A., 2020. Is the lunar magnetic field correlated with gravity or topography? J. Geophys. Res. 125 (4), e2019JE006274. http://dx.doi.org/10.1029/2019JE006274.

Halekas, J.S., Lin, R.P., Mitchell, D.L., 2003. Magnetic fields of lunar multi-ring impact basins. Meteorit. Planet. Sci. 38 (4), 565–578. http://dx.doi.org/10.1111/j.1945-5100.2003.tb00027.x.

Halekas, J.S., Mitchell, D.L., Lin, R.P., Frey, S., Hood, L.L., Acuña, M.H., Binder, A.B., 2001. Mapping of crustal magnetic anomalies on the lunar near side by the Lunar Prospector electron reflectometer. J. Geophys. Res. 106, 27,841–27,852. http://dx.doi.org/10.1029/2000JE001380.

Halekas, J.S., Mitchell, D.L., Lin, R.P., Hood, L.L., Acuña, M.H., Binder, A.B., 2002. Demagnetization signatures of lunar impact craters. Geophys. Res. Lett. 29 (13), 1–4. http://dx.doi.org/10.1029/2001GL013924.

Hemingway, D.J., Tikoo, S.M., 2018. Lunar swirl morphology constrains the geometry, magnetization, and origins of lunar magnetic anomalies. J. Geophys. Res. 123 (8), 2223–2241. http://dx.doi.org/10.1029/2018JE005604, URL http://doi.wiley.com/10.1029/2018JE005604.

Hood, L.L., 2011. Central magnetic anomalies of Nectarian-aged lunar impact basins: Probable evidence for an early core dynamo. Icarus 211 (2), 1109–1128. http://dx.doi.org/10.1016/j.icarus.2010.08.012.

Hood, L.L., Artemieva, N.A., 2008. Antipodal effects of lunar basin-forming impacts: Initial 3D simulations and comparisons with observations. Icarus 193 (2), 485–502. http://dx.doi.org/10.1016/j.icarus.2007.08.023.

Hood, L.L., Bryant, I., van der Leeuw, J., 2022. Lunar magnetic anomalies and polar ice. Geophys. Res. Lett. 49 (22), e2022GL100557. http://dx.doi.org/10.1029/2022GL100557.

Hood, L.L., Oliveira, J.S., Andrews-Hanna, J., Wieczorek, M., Stewart, S., 2021a. Magnetic anomalies in five lunar impact basins: Implications for impactor trajectories and inverse modeling. J. Geophys. Res. 126 (2), e2020JE006668. http://dx.doi.org/10.1029/2020JE006668.

Hood, L.L., Spudis, P., 2016. Magnetic anomalies in the Imbrium and Schrödinger impact basins: Orbital evidence for persistence of the lunar core dynamo into the Imbrian epoch. J. Geophys. Res. 121 (11), 2268–2281. http://dx.doi.org/10.1002/2016JE005166.

Hood, L.L., Torres, C.B., Oliveira, J.S., Wieczorek, M.A., Stewart, S.T., 2021b. A new large-scale map of the lunar crustal magnetic field and its interpretation. J. Geophys. Res. 126, http://dx.doi.org/10.1029/2020JE006667.

Isac, A., Mandea, M., Purucker, M., Langlais, B., 2016. A comparative analysis of the magnetic field signals over impact structures on the Earth, Mars and the Moon. Adv. Space Res. 57 (1), 477–492. http://dx.doi.org/10.1016/j.asr.2015.11.019, URL https://linkinghub.elsevier.com/retrieve/pii/S0273117715008169.

Kelley, M.R., Garrick-Bethell, I., 2020. Gravity constraints on the age and formation of the Moon's Reiner Gamma magnetic anomaly. Icarus 338, 113465. http://dx.doi.org/10.1016/j.icarus.2019.113465, URL https://linkinghub.elsevier.com/retrieve/pii/S0019103519304634.

Laneuville, M., Taylor, J., Wieczorek, M., 2018. Distribution of radioactive heat sources and thermal history of the Moon. J. Geophys. Res. 123 (12), 3144–3166. http://dx.doi.org/10.1029/2018JE005742.

Laneuville, M., Wieczorek, M., Breuer, D., Aubert, J., Morard, G., Rückriemen, T., 2014. A long-lived lunar dynamo powered by core crystallization. Earth Planet. Sci. Lett. 401, 251–260. http://dx.doi.org/10.1016/j.epsl.2014.05.057.

Laneuville, M., Wieczorek, M., Breuer, D., Tosi, N., 2013. Asymmetric thermal evolution of the Moon. J. Geophys. Res. 118 (7), 1435–1452. http://dx.doi.org/10.1002/jgre.20103.

Le Bars, M., Wieczorek, M.A., Karatekin, Ö., Cébron, D., Laneuville, M., 2011. An impact-driven dynamo for the early Moon. Nature 479 (7372), 215–218. http://dx.doi.org/10.1038/nature10565.

Le Feuvre, M., Wieczorek, M.A., 2011. Nonuniform cratering of the Moon and a revised crater chronology of the inner Solar System. Icarus 214 (1), 1–20. http://dx.doi.org/10.1016/j.icarus.2011.03.010.

Lillis, R.J., Frey, H.V., Manga, M., 2008. Rapid decrease in Martian crustal magnetization in the Noachian era: Implications for the dynamo and climate of early Mars. Geophys. Res. Lett. 35 (14), L14203. http://dx.doi.org/10.1029/2008GL034338, URL http://doi.wiley.com/10.1029/2008GL034338.

Lillis, R.J., Purucker, M.E., Halekas, J.S., Louzada, K.L., Stewart-Mukhopadhyay, S.T., Manga, M., Frey, H.V., 2010. Study of impact demagnetization at Mars using Monte Carlo modeling and multiple altitude data. J. Geophys. Res. 115 (E7), E07007. http://dx.doi.org/10.1029/2009JE003556, URL http://doi.wiley.com/10.1029/2009JE003556.

Lillis, R.J., Robbins, S., Manga, M., Halekas, J.S., Frey, H.V., 2013a. Time history of the Martian dynamo from crater magnetic field analysis. J. Geophys. Res. 118 (7), 1488–1511. http://dx.doi.org/10.1002/jgre.20105, URL http://doi.wiley.com/10.1002/jgre.20105.

Lillis, R.J., Stewart, S.T., Manga, M., 2013b. Demagnetization by basin-forming impacts on early Mars: Contributions from shock, heat, and excavation: Impact demagnetization on early Mars. J. Geophys. Res. 118 (5), 1045–1062. http://dx.doi.org/10.1002/jgre.20085, URL http://doi.wiley.com/10.1002/jgre.20085.

Lin, R., Mitchell, D., Curtis, D., Anderson, K., Carlson, C., McFadden, J., Acuna, M., Hood, L., Binder, A., 1998. Lunar surface magnetic fields and their interaction with the solar wind: Results from Lunar Prospector. Science 281 (5382), 1480–1484. http://dx.doi.org/10.1126/science.281.5382.1480.

Losiak, A., Kohout, T., O'Sullivan, K., Thaisen, K., Wieder, S., Öhman, T., Kring, D.A., 2015. Lunar impact crater database, third ed. Lunar and Planetary Institute, Houston, URL https://www.lpi.usra.edu/scientific-databases/.

Melosh, H.J., 1989. Impact Cratering: A Geologic Process. New York: Oxford University Press; Oxford: Clarendon Press.

Mighani, S., Wang, H., Shuster, D.L., Borlina, C., Nichols, C.I., Weiss, B.P., 2020. The end of the lunar dynamo. Sci. Adv. 6 (1), eaax0883. http://dx.doi.org/10.1126/sciadv.aax0883.

Mitchell, D., Halekas, J., Lin, R., Frey, S., Hood, L., Acuña, M., Binder, A., 2008. Global mapping of lunar crustal magnetic fields by Lunar Prospector. Icarus 194 (2), 401–409. http://dx.doi.org/10.1016/j.icarus.2007.10.027.

Mohit, P.S., Arkani-Hamed, J., 2004. Impact demagnetization of the Martian crust. Icarus 168 (2), 305–317. http://dx.doi.org/10.1016/j.icarus.2003.12.005.

Neukum, G., Ivanov, B.A., Hartmann, W.K., 2001. Cratering records in the inner solar system in relation to the lunar reference system. In: Kallenbach, R., Geiss, J., Hartmann, W.K. (Eds.), In: Chronology and Evolution of Mars, vol. 12, Springer Netherlands, Dordrecht, pp. 55–86. http://dx.doi.org/10.1007/978-94-017-1035-0_3, Series Title: Space Sciences Series of ISSI.

Neumann, G.A., 2009. Lunar orbiter laser altimeter raw data set, LRO-L-LOLA-4-GDR-V1.0. NASA Planetary Data System, http://dx.doi.org/10.17189/1520642.

Neumann, G.A., Zuber, M.T., Wieczorek, M.A., Head, J.W., Baker, D.M., Solomon, S.C., Smith, D.E., Lemoine, F.G., Mazarico, E., Sabaka, T.J., et al., 2015. Lunar impact basins revealed by gravity recovery and interior laboratory measurements. Sci. Adv. 1 (9), e1500852. http://dx.doi.org/10.1126/sciadv.1500852.

Oliveira, J.S., Wieczorek, M.A., 2017. Testing the axial dipole hypothesis for the Moon by modeling the direction of crustal magnetization. J. Geophys. Res. 122 (2), 383–399. http://dx.doi.org/10.1002/2016JE005199.

Oliveira, J.S., Wieczorek, M.A., Kletetschka, G., 2017. Iron abundances in lunar impact basin melt sheets from orbital magnetic field data. J. Geophys. Res. 122 (12), 2429–2444. http://dx.doi.org/10.1002/2017JE005397.

Oran, R., Weiss, B.P., Shprits, Y., Miljković, K., Tóth, G., 2020. Was the moon magnetized by impact plasmas? Sci. Adv. 6 (40), eabb1475. http://dx.doi.org/10.1126/sciadv.abb1475.

Pierazzo, E., Melosh, H., 2000. Melt production in oblique impacts. Icarus 145 (1), 252–261. http://dx.doi.org/10.1006/icar.1999.6332.

Pilkington, M., Grieve, R.A.F., 1992. The geophysical signature of terrestrial impact craters. Rev. Geophys. 30 (2), 161. http://dx.doi.org/10.1029/92RG00192, URL http://doi.wiley.com/10.1029/92RG00192.

Ravat, D., 2011. Interpretation of Mars southern highlands high amplitude magnetic field with total gradient and fractal source modeling: New insights into the magnetic mystery of Mars. Icarus 214 (2), 400–412. http://dx.doi.org/10.1016/j.icarus.2011.05.004.

Ravat, D., Purucker, M., Olsen, N., 2020a. Lunar magnetic field models from lunar prospector and SELENE/Kaguya along-track magnetic field gradients. J. Geophys. Res. 125 (7), e2019JE006187. http://dx.doi.org/10.1029/2019JE006187.

Ravat, D., Purucker, M.E., Olsen, N., 2020b. New magnetic field models of the moon. UKnowledge, URL https://uknowledge.uky.edu/ees_data/2/.

Robbins, S.J., 2018. Moon crater database v1 robbins. NASA Planetary Data System, URL https://astrogeology.usgs.gov/search/map/Moon/Research/Craters/lunar_crater_database_robbins_2018.

Robbins, S.J., 2019. A new global database of lunar impact craters >1–2 km: 1. Crater locations and sizes, comparisons with published databases, and global analysis. J. Geophys. Res. 124 (4), 871–892. http://dx.doi.org/10.1029/2018JE005592.

Scheinberg, A.L., Soderlund, K.M., Elkins-Tanton, L.T., 2018. A basal magma ocean dynamo to explain the early lunar magnetic field. Earth Planet. Sci. Lett. 492, 144–151. http://dx.doi.org/10.1016/j.epsl.2018.04.015.

Scheinberg, A.L., Soderlund, K.M., Schubert, G., 2015. Magnetic field generation in the lunar core: The role of inner core growth. Icarus 254, 62–71. http://dx.doi.org/10.1016/j.icarus.2015.03.013.

Stöffler, D., Ryder, G., Ivanov, B., Artemieva, N., Cintala, M., Greive, R., 2006. Cratering history and Lunar chronology. Rev. Mineral. Geochem. 60 (1), 519–596. http://dx.doi.org/10.2138/rmg.2006.60.05, URL https://pubs.geoscienceworld.org/rimg/article/60/1/519-596/140783.

Stys, C., Dumberry, M., 2020. A past lunar dynamo thermally driven by the precession of its inner core. J. Geophys. Res. 125 (7), e2020JE006396. http://dx.doi.org/10.1029/2020JE006396.

Takahashi, F., Tsunakawa, H., 2009. Thermal core-mantle coupling in an early lunar dynamo: Implications for a global magnetic field and magnetosphere of the early Moon. Geophys. Res. Lett. 36 (24), L24202. http://dx.doi.org/10.1029/2009GL041221, URL http://doi.wiley.com/10.1029/2009GL041221.

Tarduno, J.A., Cottrell, R.D., Lawrence, K., Bono, R.K., Huang, W., Johnson, C.L., Blackman, E.G., Smirnov, A.V., Nakajima, M., Neal, C.R., Zhou, T., Ibanez-Mejia, M., Oda, H., Crummins, B., 2021. Absence of a long-lived lunar paleomagnetosphere. Sci. Adv. 7 (32), eabi7647. http://dx.doi.org/10.1126/sciadv.abi7647.

Tikoo, S.M., Evans, A.J., 2022. Dynamos in the inner solar system. Ann. Rev. Earth Planet. Sci. 50, http://dx.doi.org/10.1146/annurev-earth-032320-102418.

Tikoo, S.M., Weiss, B.P., Cassata, W.S., Shuster, D.L., Gattacceca, J., Lima, E.A., Suavet, C., Nimmo, F., Fuller, M.D., 2014. Decline of the lunar core dynamo. Earth Planet. Sci. Lett. 404, 89–97. http://dx.doi.org/10.1016/j.epsl.2014.07.010.

Tikoo, S.M., Weiss, B.P., Shuster, D.L., Suavet, C., Wang, H., Grove, T.L., 2017. A two-billion-year history for the lunar dynamo. Sci. Adv. 3 (8), e1700207. http://dx.doi.org/10.1126/sciadv.1700207.

Tsunakawa, H., Shibuya, H., Takahashi, F., Shimizu, H., Matsushima, M., Matsuoka, A., Nakazawa, S., Otake, H., Iijima, Y., 2010. Lunar magnetic field observation and initial global mapping of lunar magnetic anomalies by MAP-LMAG onboard SELENE (Kaguya). Space Sci. Rev. 154 (1), 219–251. http://dx.doi.org/10.1007/s11214-010-9652-0.

Tsunakawa, H., Takahashi, F., Shimizu, H., Shibuya, H., Matsushima, M., 2015. Surface vector mapping of magnetic anomalies over the Moon using Kaguya and Lunar Prospector observations. J. Geophys. Res. 120 (6), 1160–1185. http://dx.doi.org/10.1002/2014JE004785.

Vervelidou, F., Lesur, V., Grott, M., Morschhauser, A., Lillis, R.J., 2017. Constraining the date of the Martian Dynamo Shutdown by means of crater magnetization signatures. J. Geophys. Res. 122 (11), 2294–2311. http://dx.doi.org/10.1002/2017JE005410, URL http://doi.wiley.com/10.1002/2017JE005410.

Weiss, B.P., Tikoo, S.M., 2014. The lunar dynamo. Science 346 (6214), 1246753. http://dx.doi.org/10.1126/science.1246753.

Wieczorek, M.A., 2018a. Spherical harmonic model of the Moon's magnetic field derived from gridded data in Tsunakawa others, (2015). Zenodo, http://dx.doi.org/10.5281/zenodo.3873648.

Wieczorek, M.A., 2018b. Strength, depth, and geometry of magnetic sources in the crust of the Moon from localized power spectrum analysis. J. Geophys. Res. 123 (1), 291–316. http://dx.doi.org/10.1002/2017JE005418.

Wieczorek, M.A., Neumann, G.A., Nimmo, F., Kiefer, W.S., Taylor, G.J., Melosh, H.J., Phillips, R.J., Solomon, S.C., Andrews-Hanna, J.C., Asmar, S.W., et al., 2013. The crust of the Moon as seen by GRAIL. Science 339 (6120), 671–675. http://dx.doi.org/10.1126/science.1231530.

Wieczorek, M.A., Weiss, B.P., Breuer, D., Cébron, D., Fuller, M., Garrick-Bethell, I., Gattacceca, J., Halekas, J.S., Hemingway, D.J., Hood, L.L., Laneuville, M., Nimmo, F., Oran, R., Purucker, M.E., Rückriemen, T., Soderlund, K.M., Tikoo, S.M., 2022. Lunar magnetism. URL https://hal.science/hal-03524536.

Wieczorek, M.A., Weiss, B.P., Stewart, S.T., 2012. An impactor origin for lunar magnetic anomalies. Science 335 (6073), 1212–1215. http://dx.doi.org/10.1126/science.1214773.

Wilhelms, D.E., McCauley, J.F., Trask, N.J., 1987. The geologic history of the Moon.

Wünnemann, K., Collins, G., Melosh, H., 2006. A strain-based porosity model for use in hydrocode simulations of impacts and implications for transient crater growth in porous targets. Icarus 180 (2), 514–527. http://dx.doi.org/10.1016/j.icarus.2005.10.013.

Yang, X., Wieczorek, M.A., 2024. Magnetic Signatures of Lunar Impact Craters. Zenodo, http://dx.doi.org/10.5281/zenodo.10795394.

Zhang, N., Parmentier, E., Liang, Y., 2013. A 3-D numerical study of the thermal evolution of the Moon after cumulate mantle overturn: The importance of rheology and core solidification. J. Geophys. Res. 118 (9), 1789–1804. http://dx.doi.org/10.1002/jgre.20121.

Zhu, M.-H., Artemieva, N., Morbidelli, A., Yin, Q.-Z., Becker, H., Wünnemann, K., 2019. Reconstructing the late-accretion history of the Moon. Nature 571 (7764), 226–229. http://dx.doi.org/10.1038/s41586-019-1359-0, URL http://www.nature.com/articles/s41586-019-1359-0.